Bio-Design and Manufacturing (2020) 3:361–372
https://doi.org/10.1007/s42242-020-00085-5

RESEARCH ARTICLE

3D bioprinted breast tumor model for structure–activity relationship study

Xiaorui Li[1] · Quanfeng Deng[2] · Tiantian Zhuang[1] · Yao Lu[3] · Tingjiao Liu[4] · Weijie Zhao[1] · Bingcheng Lin[3] · Yong Luo[1] · Xiuli Zhang[2]

Received: 14 April 2020 / Accepted: 16 June 2020 / Published online: 9 July 2020

Abstract

In this paper, we present a 3D printed tumor spheroidal model suitable for drug discovery. This model is based on a hydroxyethyl cellulose/alginate/gelatin (HCSG) composite biomaterial that has three distinct properties: (1) the HCSG is similar to the commercial basement membrane extract in Ki67, MUC1, and PARP1 expressions of MCF-7 cells for embedding culture; (2) the HCSG is printable at room temperature; and (3) the HCSG can be large-scale manufactured at an ultralow cost.We printed a 3D MCF-7 spheroid model with HCSG and characterized it in terms of cell viability, spheroid size, key protein expression, and mitochondrial metabolic activity. We used the 3D MCF-7 spheroid model to evaluate the anti-breast cancer activity of 13 amino acid-based flavone phosphoramidates and found that the alanine structure induced a stronger drug resistance, whereas phenylalanine hardly caused drug resistance in the MCF-7 cells. This is the first time that 3D bioprinting technology has been used in a structure–activity relationship study.

Keywords Biomaterial · Structure–activity relationship · Hydroxyethyl cellulose

Introduction

In the development of a commercial drug, late-stage failures have frequently occurred due to either efficacy or toxicity issues, which wastes massive amounts of time and financial resources. Adoption of new techniques in the drug discovery pipeline has been regarded as a solution to this serious issue. Typically, artificial intelligence [1], cell spheroid model [2], organ-on-a-chip [3], organoid [4], 3D bioprinting [5], and similar techniques have been gradually merged into the pharmaceutical industry to increase the efficiency of drug discovery. Among them, the 3D bioprinting technique offers highly biomimetic in vitro models and has attracted considerable attention.

Sun et al. developed an in vitro cervical tumor model by 3D extrusion bioprinting. The viability of HeLa cells encapsulated in alginate/gelatin/fibrinogen hydrogels was ~ 90% after extrusion. During the culture process, cells within 3D hydrogels automatically formed spheroids. Compared to 2D planar samples, 3D printed constructs were found to be more chemoresistant to paclitaxel [6]. Scaffold-free human breast cancer cells were bioprinted to test the chemotherapeutic effects of tamoxifen using the Organovo's NovoGen BioprintingTM platform in which cancer cells were encapsulated

Xiaorui Li and Quanfeng Deng have contributed equally to this work.

Electronic supplementary material The online version of this article (https://doi.org/10.1007/s42242-020-00085-5) contains supplementary material, which is available to authorized users.

✉ Bingcheng Lin
bclin@dicp.ac.cn

✉ Yong Luo
yluo@dlut.edu.cn

✉ Xiuli Zhang
zhangxl@suda.edu.cn

[1] Present Address: State Key Laboratory of Fine Chemicals, Department of Pharmaceutical Sciences, School of Chemical Engineering, Dalian University of Technology, Dalian, China

[2] Present Address: College of Pharmaceutical Sciences, Soochow University, Soochow, China

[3] Present Address: Dalian Institute of Chemical Physics, Chinese Academy of Sciences, Dalian, China

[4] Section of Oral Pathology, College of Stomatology, Dalian Medical University, Dalian, China

by a biomimetic extracellular matrix (ECM) consisting of marrow mesenchymal stem cell-derived mammary fibroblasts and endothelial and adipose cells [7]. Recently, Kundu reviewed the research progress on 3D tumor models and concluded that 3D in vitro cancer models can improve the predictability of toxicity and drug sensitivity in cancer; however, they still have not reached the standardization required for preclinical trials [8].

In this paper, we present a new 3D tumor model for preclinical trial, and we use it in structure–activity relationship study as a demonstration. Many drug candidates, especially those from natural products, have the same molecular skeletons but vary in their substitutional atomic groups, for example, quinoline alkaloids [9]. These atomic groups substantially affect the activity of the drug candidates. The relationship between the activities of drug candidates and substituents is termed as "structure–activity relationship (SAR)." For example, Dirk Vanden Berghe et al. measured the half-maximal inhibitory concentrations of a series of flavonoids as inhibitors of xanthine oxidase and superoxide scavengers and identified the SAR of these flavonoids [10]. The SAR is not only the key to many aspects of new drug development ranging from primary screening to lead optimization but is also useful in the prediction of chemical toxicity and assessment of side effect health risks posed by existing compounds. The results of an SAR study directly determine the structural orientation of the candidate compounds, affecting the efficiency of new drug development.

Recently, 3D cell models, as a replacement for traditional 2D planar models, started to be used in SAR studies. For example, Xiuli Zhang et al. attempted to study the SAR of bufadienolides as anti-gastric cancer agents by using the technology of three-dimensional matrixless tumor spheroids [11]. They found that the SAR results obtained varied with those from a traditional 2D planar cell model. However, due to a lack of extracellular matrix, the matrixless tumor spheroid model is not highly biomimetic. The matrix-based 3D tumor model can be constructed by 3D bioprinting technology [12–15]; however, it thus far has not been used in an SAR study.

In this study, we printed a spider web-like 3D breast tumor model featuring the hydroxyethyl cellulose/alginate/gelatin (HCSG) composite biomaterial. HCSG is an alternative to commercial BME, which can be easily manufactured and standardized. Then, we used the 3D breast tumor model to study the SAR of 13 flavone phosphoramidates and found that the alanine structure induced a stronger drug resistance, whereas phenylalanine hardly caused drug resistance in MCF-7 cells.

Materials and methods

Cell culture

The MCF-7 cells were obtained from Dalian Medical University. The cells were cultured in Dulbecco's modified Eagle medium (DMEM; HyClone) with 10% newborn calf serum (NBCS; HyClone) and 1% penicillin/streptomycin (HyClone) in a CO_2 incubator at 37 °C at 5% CO_2. The MCF-7 cells were dissociated by trypsin [0.25% in phosphate buffer saline (PBS)] at ~ 90% confluence. The culture media were changed every 2–3 days.

Matrix preparation

Gelatin powder (Amersco, 9764), sodium alginate powder (Sigma, A0682), and hydroxyethyl cellulose (HEC; Aldrich, 434965) were exposed to ultraviolet light overnight and then dissolved in normal saline. Gelatin and sodium alginate mixed to form a composite gel of sodium alginate/gelatin (SG) with a sodium alginate concentration of 1% (w/v) and gelatin concentration of 5% (w/v). We added 1% (w/v) HEC to SG to form a composite gel of hydroxyethyl cellulose/sodium alginate/gelatin (HCSG). The solutions were sterilized by heating in a stove (70 °C) for 1 h and cooling at room temperature for 2 h, and the sterilization was repeated 3 times. $CaCl_2$ (Sigma, C7902) was dissolved in DMEM at 1.5% (w/v).

Printability test at different temperatures and mechanical property test

We printed SG and HCSG with a homemade extrusion-based bioprinter. The red ink and gel were mixed at a volume ratio of 1:10, followed by incubation of the gel suspension for 15 min to remove air bubbles. Then, the 1.5-mL gel suspension was loaded into the printing cartridge and physically cross-linked for 15 min. With a printing moving speed of 5 mm/s and an electric extrusion speed of 6 mm/s, a spider web-like decagon was printed that was 5 mm wide and 1 mm high at temperatures of 10 °C, 15 °C, 25 °C and 37 °C.

The MCF-7 cell suspension was mixed with SG and HCSG at a volume ratio of 1:10, respectively. The SG and HCSG suspension of MCF-7 cells was applied at different temperatures for 30 min to measure the MCF-7 cell viability. We then loaded the SG and HCSG suspension of MCF-7 cells into the printing cartridge and printed at different temperatures. The printed samples were ion cross-linked with 1.5% $CaCl_2$ for 1 min, followed by washing with DMEM medium 3 times and tested for cell viability.

The rheological behavior of the gel solution was measured using a rheometer (TA Instruments, AR2000ex) equipped with a Peltier plate thermal controller at 25 °C. To evaluate the storage modulus (G') and loss modulus (G''), angle frequency sweep experiments were performed by varying angle frequencies from 1 to 100 rad/s at a fixed strain of 0.5%. The compressive modulus of the alginate and alginate-gelatin samples was tested using an MTS mechanical tester. The ink solutions were cast in custom-made molds (cylindrical, 9 mm diameter, 8 mm in height) and then cross-linked by 1.5% $CaCl_2$ for 1 min and washed with DMEM for 3 × 5 min. Each sample was tested at a strain rate of 1 mm/min and fitted in a 100-N load cell. The compression modulus was determined as the slope of the stress–strain curve at 0-10% strain.

Construction of the MCF-7 spheroid model

The 2D monolayer culture was realized by seeding MCF-7 cells at a density of 5000 cells/well in 96-well plates using 200 μL of culture media.

The MCF-7 cells embedded in BME (Gibco, A1413201) were placed on ice. The cell suspension and BME were mixed at a volume ratio of 1:1, and the final density was 10^7 cells/mL. A 13 μL mixture of BME and cells was added to 48-well plates, jelled in an incubator for 15 min, and then cultured with 300 μL of culture media per well.

MCF-7 cells were cultured in 6-well plates with an ultralow attachment surface at a density of 3000 cells/well with 2 mL of culture media (supplemented with 500 μL every 2–3 days). The culture medium was DMEM supplemented with 20 ng/mL of epidermal growth factor (Sigma, E9644), 20 ng/mL basic fibroblast growth factor (PeproTech, 100-18B) and 2% B-27 Supplement (Gibco, 17504044). MCF-7 matrixless spheres with a size of 200 μm formed after 3 days.

To fabricate the MCF-7 cells embedded in the HCSG model, the 13 μL mixture of gel and cells was added to 48-well plates that were preloaded with 200 μL $CaCl_2$ solution for 1 min, washed in DMEM for 3 × 5 min, and then cultured with 300 μL of culture media per well.

We fabricated the 3D bioprinted MCF-7 tumor spheroid model using a homemade extruded bioprinter. After digestion, the MCF-7 cells were collected by centrifuge at 1000 r/min for 4 min and resuspended in culture medium. The cell suspension and HCSG were mixed at a volume ratio of 1:10, and the final density in the gel suspension was 10^7 cells/mL, followed by incubation of the gel suspension for 15 min to remove air bubbles. Then, 3 mL of the gel suspension was loaded into the printing cartridge and physically cross-linked for 15 min. A spider web-like decagon was fabricated that was 5 mm wide and 1 mm high at 20 °C, and then it was ion cross-linked with 1.5% $CaCl_2$ for 1 min. Then, the decagon was gently washed in DMEM for 3 × 5 min and cultured in 48-well plates with 300 μL of culture media per well.

Protein expression assay

The MCF-7 cells in the bioprinted model were fixed by 4% paraformaldehyde for 10 min at room temperature, washed twice with PBS, permeabilized in 0.1% Trion X-100 for 5 min at room temperature, and washed twice with PBS. Then, we added phalloidin (Invitrogen) at 1/200 dilution and incubated it overnight at 4 °C. The samples were washed at 3 × 5 min in PBS, followed by 100 nmol/L DAPI for 2 min, and then imaged using an inverted fluorescence microscope and analyzed with Image ProPlus.

The samples of MCF-7 cells embedded in the HCSG and BME model were fixed by 100% cold methanol for 10 min at room temperature, washed twice with PBS, permeabilized in 0.1% Trion X-100 for 5 min at room temperature, washed for 3 × 5 min with PBS, and blocked with 1% bovine serum B (BSA) in 0.1% PBS-tween for 1 h. Then, we added anti-Ki67 (ab197234) or anti-MUC1 (ab223134) at 1/100 dilution and incubated overnight at 4 °C. The samples were washed for 3 × 5 min in PBS prior to counterstaining the DNA with 200 μL of 100 nmol/L 4′,6-diamidino-2-phenylindole (DAPI) (Sigma, D8417) in PBS and then imaged using an inverted fluorescence microscope and analyzed with Image ProPlus.

The MCF-7 cell samples embedded in the HCSG and BME model were fixed by 4% paraformaldehyde for 10 min at room temperature, washed twice with PBS, permeabilized in 0.1% Trion X-100 for 5 min at room temperature, and washed twice with PBS. Then, we added anti-PARP1 (ab191217) at 1/500 dilution and incubated overnight at 4 °C. The samples were washed for 3 × 5 min in PBS, followed by Goat Anti-Rabbit IgG H&L (ab150079) at 1/500 dilution for 1 h in the dark at room temperature. The samples were washed for 3 × 5 min in PBS prior to counterstaining the DNA with 200 μL of 100 nmol/L DAPI in PBS and then imaged using an inverted fluorescence microscope and analyzed with Image ProPlus.

Cell live–dead assay

We assessed the cell survival in the bioprinted model and HCSG monolithic model from day 1 to day 15. The samples were stained in an incubator using a live–dead assay kit (KGAF001) for 30 min in which Calcein-AM was 2 μmol/L and propidium iodide (PI) was 4 μmol/L. Then, the samples were washed with PBS for 3 × 5 min and observed using an inverted fluorescence microscope (Olympus IX71).

Cell mitochondrial metabolic activity monitoring

The cell proliferation of the bioprinted model and HCSG monolithic model was measured by MTT (Sigma, M5655). First, 30 μL of MTT (5 mg/mL) was added into the 48-well plates and incubated in the dark at 37 °C for 4 h. Then, the MTT solution was gently pipetted out and 800 μL of gel lysis solution [0.055 mol/L of sodium citrate (Sigma, S4651)] and 0.02 mol/L of ethylenediaminetetraacetic acid disodium salt (Sigma, E6635) were added to the well for 10 min to dissolve the gel. We collected the gel lysis solution into a 1.5-mL centrifuge tube and centrifuged at 50,000 r/min for 3 min; then, the supernatant was discarded, and we added 800 μL of dimethyl sulfoxide (DMSO) to dissolve the purple crystals. Finally, 150 μL of DMSO solution was transferred to the 96-well plates, and the absorbance value was read using a microplate reader (Gene) at 490 nm. Four independent samples were tested in each group.

SAR study of 13 isoflavone derivatives on MCF-7 cells

In total, the 13 compounds were all isoflavone-7-phosphoramidate derivatives. The concentrations of the compounds were 1, 5, 15, 30, 60, and 100 μmol/L against the 2D monolayer model and 30, 60, 100, 150, and 200 μmol/L against the bioprinted model. The models were incubated with different concentrations of isoflavones for 72 h; then, we measured the absorbance values as mentioned before. The inhibition rate was calculated as follows: IR = (ODc-ODm)/(ODc-ODo) × 100%, where IR, ODc, ODm, and ODo were the inhibition rate, the absorbance value at 0 μmol/L concentration, the absorbance value at different concentrations, and the absorbance value of DMSO, respectively. We plotted the inhibitory rate–concentration curve and calculated the concentration of 50% inhibition (IC_{50}) using probit regression. Then, the SARs of the isoflavone against the MCF-7 cells in the 2D monolayer model and spheroids model were compared using the IC_{50}.

Statistical analysis

All data are presented as the mean ± standard deviation ($n = 4$). Statistical significance was determined by Student's t test using IBM SPSS Statistics, and p values of less than 0.05 were considered statistically significant.

Results

Hydroxyethyl cellulose/sodium alginate/gelatin (HCSG) composite biomaterial

We investigated whether the three-dimensional structure can be successfully printed according to the design under different printing temperatures, that is, the printability of the design structure. Figure 1a shows that hydroxyethyl cellulose/sodium alginate/gelatin (HCSG) can be printed at 25 °C. At this temperature, the viability of MCF-7 cells in printed HCSG was as high as 98% (Fig. 1b). As a comparison, the SG was a liquefied hydrogel at 25 °C, which could not be 3D printed (Fig. 1a), and the optimal printing temperature for SG was ~ 10 °C. However, at this temperature, the viability of MCF-7 cells in printed SG was less than 65% (Fig. 1b). Additionally, as shown in Fig. 1b, the viability of the MCF-7 cells in the printed HCSG and monolithic HCSG was the same regardless of the printing temperature, which indicated that the printing process did not affect the viability of MCF-7 cells.

We also studied the rheological properties of HCSG with SG as the control, as shown in Fig. 1c. The "$G' - \omega$" curve of HCSG was above the "$G'' - \omega$" curve of HCSG, which indicated that HCSG exhibited gel-like behavior. Additionally, the "$G' - \omega$" curves of HCSG were all higher than that of SG, indicating that HCSG has a higher viscoelastic modulus than SG to hold the complex ear-like 3D structure, as shown in Fig. 1e. Figure 1d shows that the compressive stress–strain curve of cross-linked HCSG is above that of cross-linked SG, which indicates that the compressive rupture strength of cross-linked HCSG is greater than that of cross-linked SG. We calculated the compressive modulus as the slope of the linear region corresponding to 0–10% strain. The compressive modulus of cross-linked HCSG (13.0 kPa) is ~ 1.6 times that of cross-linked SG (7.9 kPa), indicating that cross-linked HCSG has a greater stiffness and is easier to shape and translocate.

Ki67 is a nuclear protein associated with cell proliferation [16, 17]. MUC1, which is highly expressed in cancer cells, can promote cancer cell invasion, resulting in the promotion of cancer metastasis [18]. PARP1, an enzyme that repairs single-stranded DNA breaks, is abundantly expressed in breast cancer [19]. We also investigated Ki67, MUC1, and PARP1 expression of MCF-7 cells in the HCSG compared that in the BME as the control, as shown in Fig. 2. The difference in Ki67, MUC1, and PARP1 expressions between in HCSG and in BME fluctuated over time in a small range. The average differences of Ki67, MUC1, and PARP1 expressions in HCSG and in BME were ~ 1.5%, ~ 2.0%, and ~ 4.4%, respectively. These

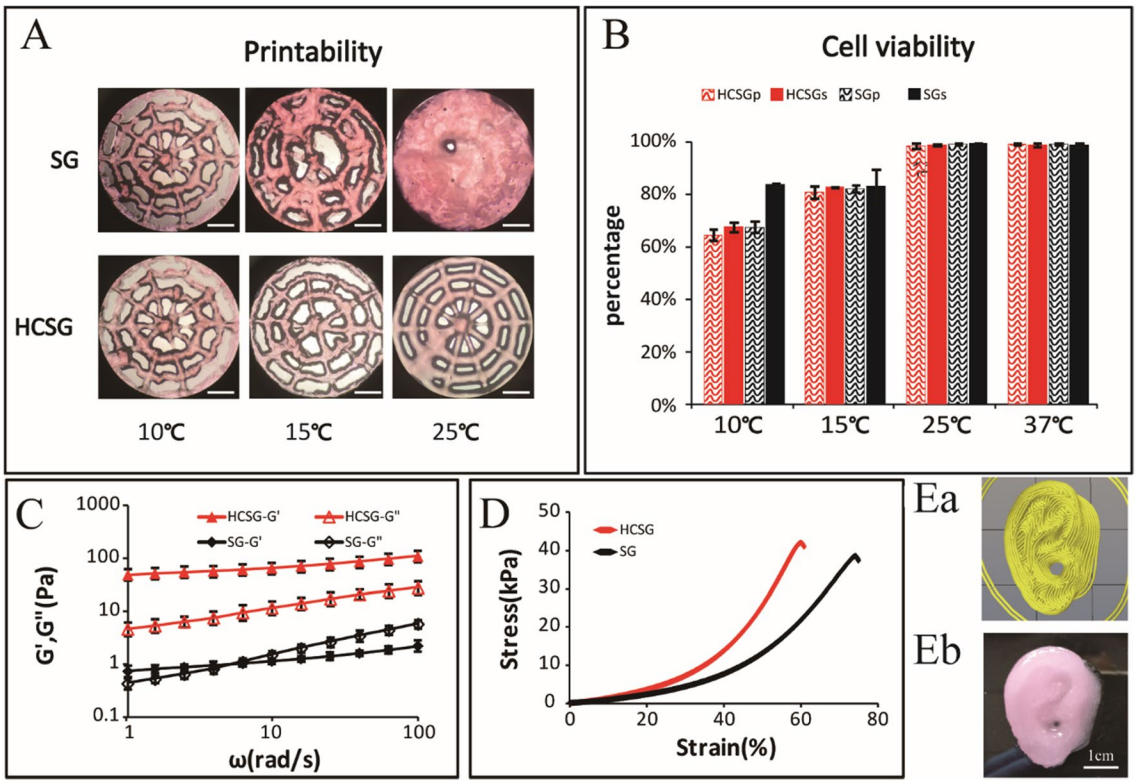

Fig. 1 Comparison of SG and HCSG in terms of printing temperature, rheological behavior, and mechanical property. **a** Morphologies of the printed SG and HCSG at different temperatures, scale bar = 1 mm; **b** Survival rates of MCF-7 cells at 10 °C, 15 °C, 25 °C, and 37 °C in SGs, SGp, HCSGs, and HCSGp, respectively. SGs: MCF-7 cell suspension in SG monolith, HCSGs: MCF-7 cell suspension in HCSG monolith, SGp: MCF-7 cells in printed SG, HCSGp: MCF-7 cells in printed HCSG; **c** Rheological behavior of SG and HCSG, where G' is the storage modulus, G'' is the loss modulus and ω is the angular frequency; **d** Compressive stress–strain curves of cross-linked HCSG and SG; **e** Printed ear-like 3D structure with HCSG, where Ea is the design image, Eb is the object picture. Rheological behavior of SG and HCSG. All data are presented as the mean ± standard deviation ($n = 4$)

statistical data revealed that Ki67, MUC1, and PARP1 expressions in HCSG and in BME were similar. The similar expression intensity of Ki67 indicated that the effect of HCSG on cell proliferation was the same as that of commercial BME on cell proliferation. The glycosylation of MUC1 can inhibit chemotherapeutic drugs reaching their targets in cells. The similar expression intensity of MUC1 indicated that HCSG was similar to BME in terms of resistance to drugs. The similar intensity of PARP1 expression further demonstrated that the physiology of MCF-7 cells in HCSG was similar to that in commercial BME.

Establishment of the HCSG-based bioprinted MCF-7 spheroid model

As mentioned in Hydroxyethyl cellulose/sodium alginate/gelatin (HCSG) composite biomaterial section, the features of HCSG are: (1) that it has a good printability and biocompatibility; (2) that the key protein expressions of tumor cells are basically the same as those in BME; (3) that the printing temperature is room temperature, thus promising the high viability of the printed cells; and (4) that it is cost-effective and easy to obtain from nature. Thus, HCSG is suitable for establishing highly biomimetic 3D bioprinted MCF-7 spheroid models for drug discovery.

We loaded a mixture of HCSG and MCF-7 cells into the syringe in a laboratory-made bioprinter and printed a spider web-like decagon as a MCF-7 spheroid model (Fig. 3). The spider web-like model has two advantages: (1) it has a large surface-to-volume ratio, which facilitates the proliferation and aggregation of tumor cells and (2) the pores of the spider web functionally simulate the vessels in a tumor. Both are responsible for mass transfer and nutrition supply in tumor models. The height and width of the decagon were 1 and 5 mm, respectively. The diameters of the three concentric circles were 2.5, 3.8, and 5 mm. All the lines in the decagon were 250 μm wide. Figure 4e–g shows the state of the cells in the "spider web" at different temporal points. At the initial stage, MCF-7 cells were dispersed in the gel; however, after 7 days of culturing, they aggregated resembling a breast tumor in the body.

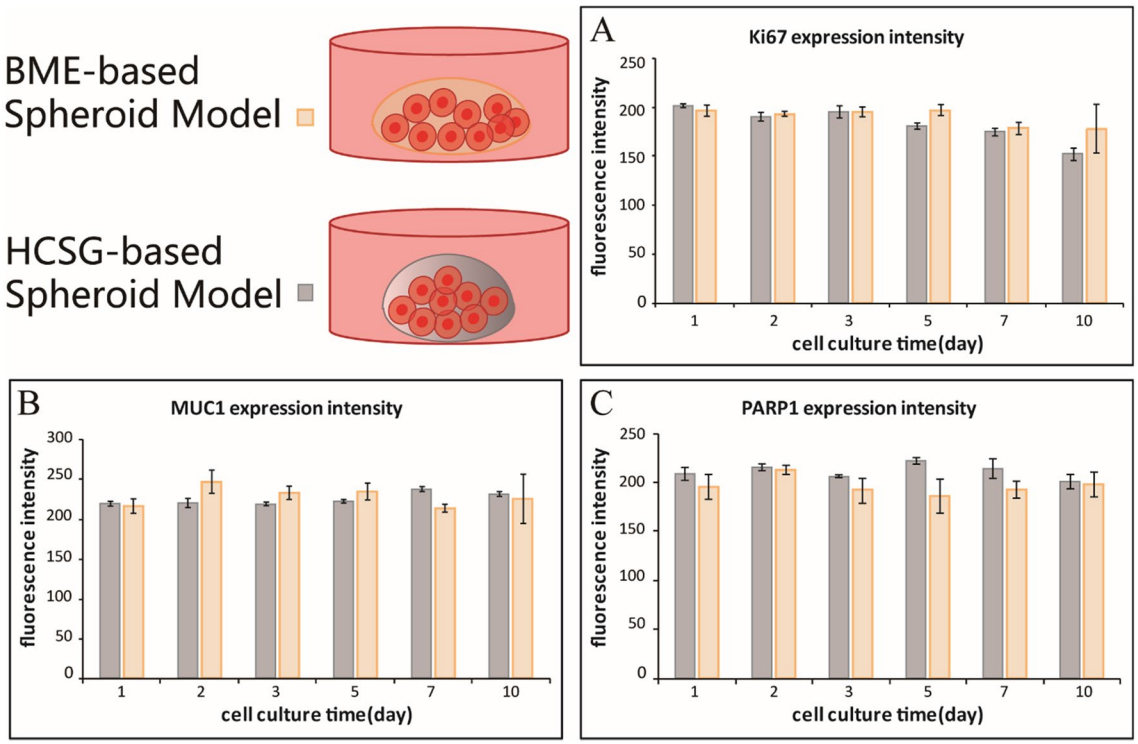

Fig. 2 Protein expressions in MCF-7 cells embedded in HCSG and commercial BME. **a** Ki67 expression in HCSG (gray) and BME (orange); **b** MUC1 expression in HCSG and BME; **c** PARP1 expression in HCSG and BME. All data are presented as the mean ± standard deviation ($n = 4$)

Physiology of MCF-7 spheroids in the HCSG-based bioprinted model

HCSG-based monolithic model was of MCF-7 cells embedded in casted HCSG gel. According to prior reports [20, 21], the structure of the gel affects the activities of cells they are embedded in. We studied the viability, proliferation, and metabolism of MCF-7 spheroids in the HCSG-based bioprinted model compared with those in the HCSG monolith as a control. We took fluorescence images of the MCF-7 spheroids in the HCSG-based bioprinted and monolithic models from day 1 to day 15, as shown in Fig. 4a. Qualitatively, the sizes of the spheroids from the printed model were larger than those from the monolithic model. We quantitatively analyzed Fig. 4a, and the results are shown in Fig. 4b, c. The viabilities of the spheroids in the bioprinted and monolithic models were the same, which were as high as ~ 98%; however, the spheroid size in the bioprinted model was bigger than that in the monolithic model regardless of the temporal point, which implied that the cell proliferation in the bioprinted model was more active than that in the monolithic model. Figure 4d shows the Ki67 protein expression intensities in the bioprinted and monolithic models. The Ki67 protein expression was more intensive in the bioprinted model than that in the monolithic model, which further verified that the proliferation of MCF-7 spheroids in the bioprinted model was more active than that in the monolithic model. As shown in Fig. 4e, the mitochondrial metabolic activities of MCF-7 cells in the bioprinted and monolithic models were almost the same in the initial 2-day culture; however, from day 3, the bioprinted model started to surpass the monolithic model significantly. The mitochondrial metabolic activity of MCF-7 spheroids in the bioprinted model was larger than that in the monolithic model.

SAR of 13 isoflavone derivatives measured using the HCSG-based 3D bioprinted MCF-7 spheroid model

We evaluated the inhibition cell proliferation of 13 flavone-7-phosphoramidate derivatives (see Table S1 in supporting information, named as 1a, 1b, 1c, 1d, 2c, 2d, 3a, 3b, 3c, 3d, 4a, 4b, and 4c) using the HCSG-based 3D bioprinted MCF-7 spheroid model compared with the 2D monolayer model, as shown in Fig. 5 and Table 1. The inhibitory potency measured using the 3D bioprinted spheroid model was different from that with the 2D cell monolayer model.

First, in the 3D bioprinted model, the dose–response curve of the compound conforms to the S curve, from which we could calculate the IC_{50} value of each compound; thus, this 3D bioprinted model can be used as a model to evaluate the activity against breast cancer. In addition, the IC_{50}

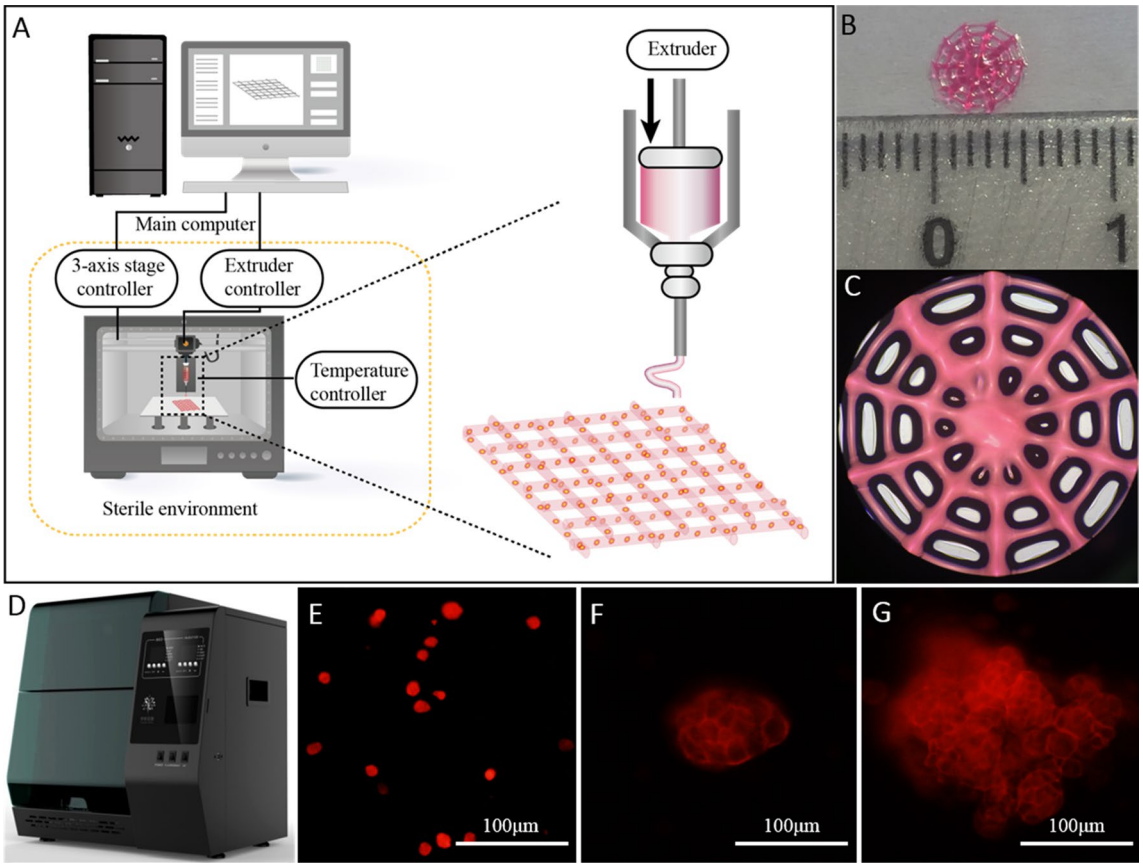

Fig. 3 3D bioprinted MCF-7 cell model. **a** Schematic of the extrusion-based bioprinter; **b**, **c** Appearance of the 3D bioprinted MCF-7 model; **d** Image of the laboratory-made bioprinter; **e**–**g** F-actin fluorescent images of MCF-7 cells in the 3D bioprinted model stained with phalloidin with E, day 1; F, day 7; G, day 15

values of the three anticancer drugs in the HCSG 3D spheres were greater than those from the 2D model. This result is more common in the 3D model. The cells in the center of the ball may have certain tumor stem cell characteristics and enhanced anti-killing ability.

Second, when the IC_{50} (3D) of other compounds is greater than the IC_{50} (2D), the IC_{50} (3D) of compound 3a does not increase but decreases slightly, indicating that the compound retains the same killing ability for globular MCF-7 cells. In fact, the IC_{50} (3D)/IC_{50} (2D) values of the three flavonoid derivatives (1a, 3a, and 4a) modified by Phe are significantly smaller than those of the three clinical drugs.

Third, according to the 3D evaluation, 10 compounds had IC_{50} values less than erlotinib and fluorouracil (5-FU) (two positive control), whereas according to the 2D results, only compounds 1d, 2d, and 3d were slightly better than erlotinib.

Additionally, these compounds were tested against the activity of HepG2, and we compared the IC_{50} values of the 13 compounds against two cancers to determine the selectivity of the compounds [22]. Eight of the 13 compounds had similar IC_{50} in both cells. Specifically, 2d, 1a, 1b, and 2c inhibited MCF-7 more than HepG2 cells, and only the 3d compound had a higher activity on HepG-2; however, none of 3a, 3b, and 3c, which had the same daidazein in the nucleus, showed a high selectivity to HepG2. Thus, the selective structural law could not be obtained.

The SAR of the amino acid skeleton and isoflavone bone structure based on the 3D bioprinted MCF-7 spheroid model was different from that based on the 2D MCF-7 monolayer model. The SAR data obtained with the "HCSG spider web" revealed that the anticancer activity of acetylated isoflavone was highest when the substitutional amino acid group was phenylalanine. However, the SAR data obtained with the traditional nonbiomimetic 2D monolayer culture showed that it was alanine. This suggested that drug molecules display different pharmacologies against 3D bioprinted models compared with that against a 2D monolayer culture. This phenomenon has also been reported elsewhere [11], possibly due to changes in cell phenotypes.

We also tested the influence of microenvironments on the SAR study. We observed that, for the same drug candidates (1c, 1d, 2c), the SAR results varied between these three tumor spheroid models. The essential difference between these three spheroid models was the microenvironment, as

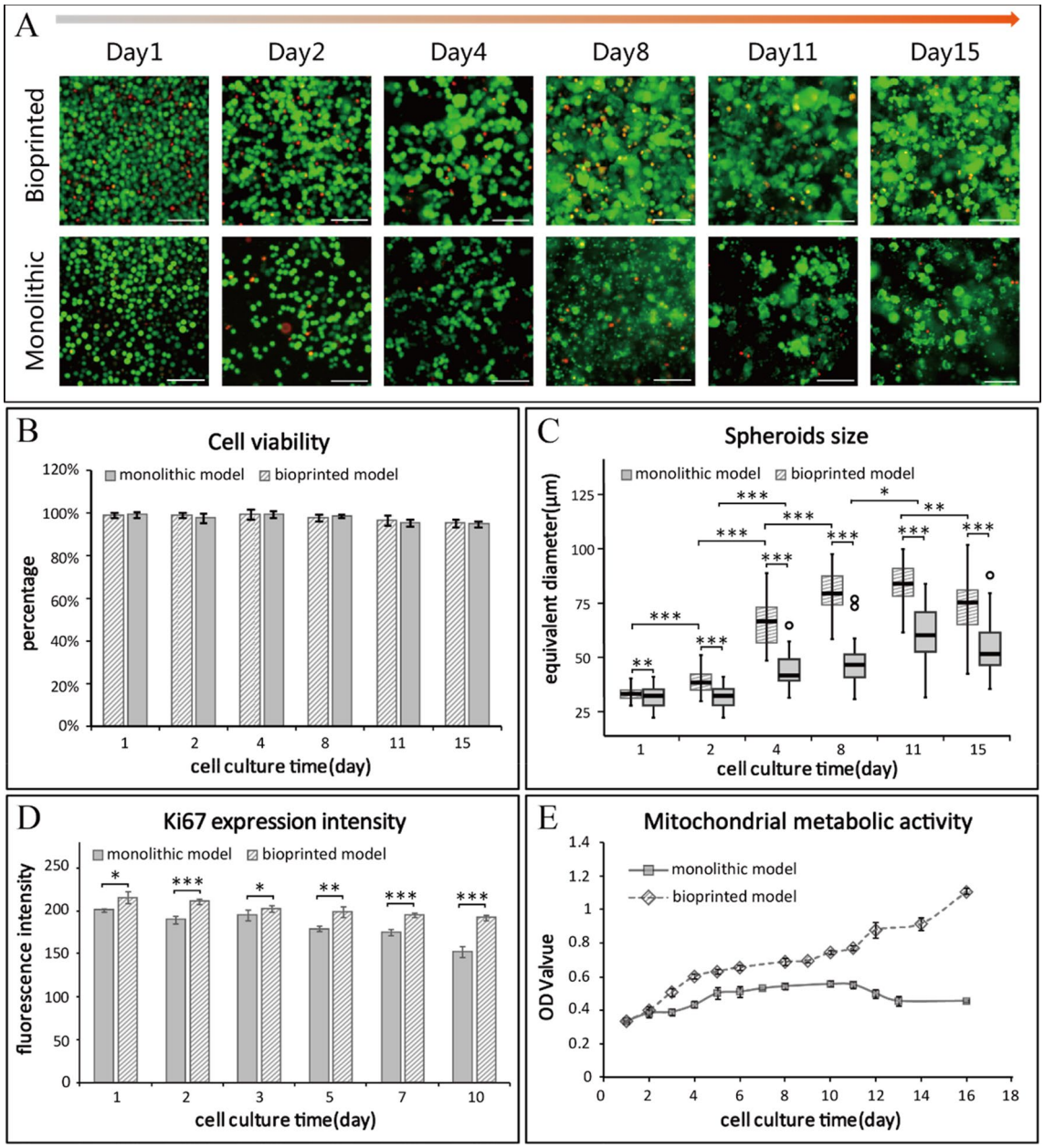

Fig. 4 **a** Fluorescence images of live and dead MCF-7 cells in the bioprinted and monolithic models from day 1 to day 15, Calcein-AM (green) and PI (red), scale bar = 100 μm; **b** time-resolved cell viability of the MCF-7 cells in the printed and monolithic models; **c** time-resolved spheroids size in the printed and monolithic models; **d** time-resolved Ki67 expression intensity of the MCF-7 cells in the printed and monolithic models; **e** time-resolved mitochondrial metabolic activity of the MCF-7 cells in the printed and monolithic models. All the data are presented as the mean ± standard deviation ($n = 4$), *($0.01 < P < 0.05$), **($0.001 < P < 0.01$),*** ($P < 0.001$)

listed in Table 2. The HCSG-based bioprinted MCF-7 spheroid model was the most biomimetic model among them. We also tested the stability of the tumor spheroid models upon interacting with drugs. We observed that the matrix-less spheroid model was not stable when interacting with the drug (Fig. S2 in the supporting information). However, we did not observe the disintegration of the tumor spheroids in the HCSG-based bioprinted MCF-7 spheroid models.

Discussion

The SAR plays an important role in drug discovery. A trend in modern drug discovery is adoption of state-of-the-art technologies, such as organ-on-a-chip, organoids, artificial intelligence, and 3D cell cultures. This study attempted to develop a more suitable in vitro cell model for an SAR study. This model meets the following requirements: (1) it

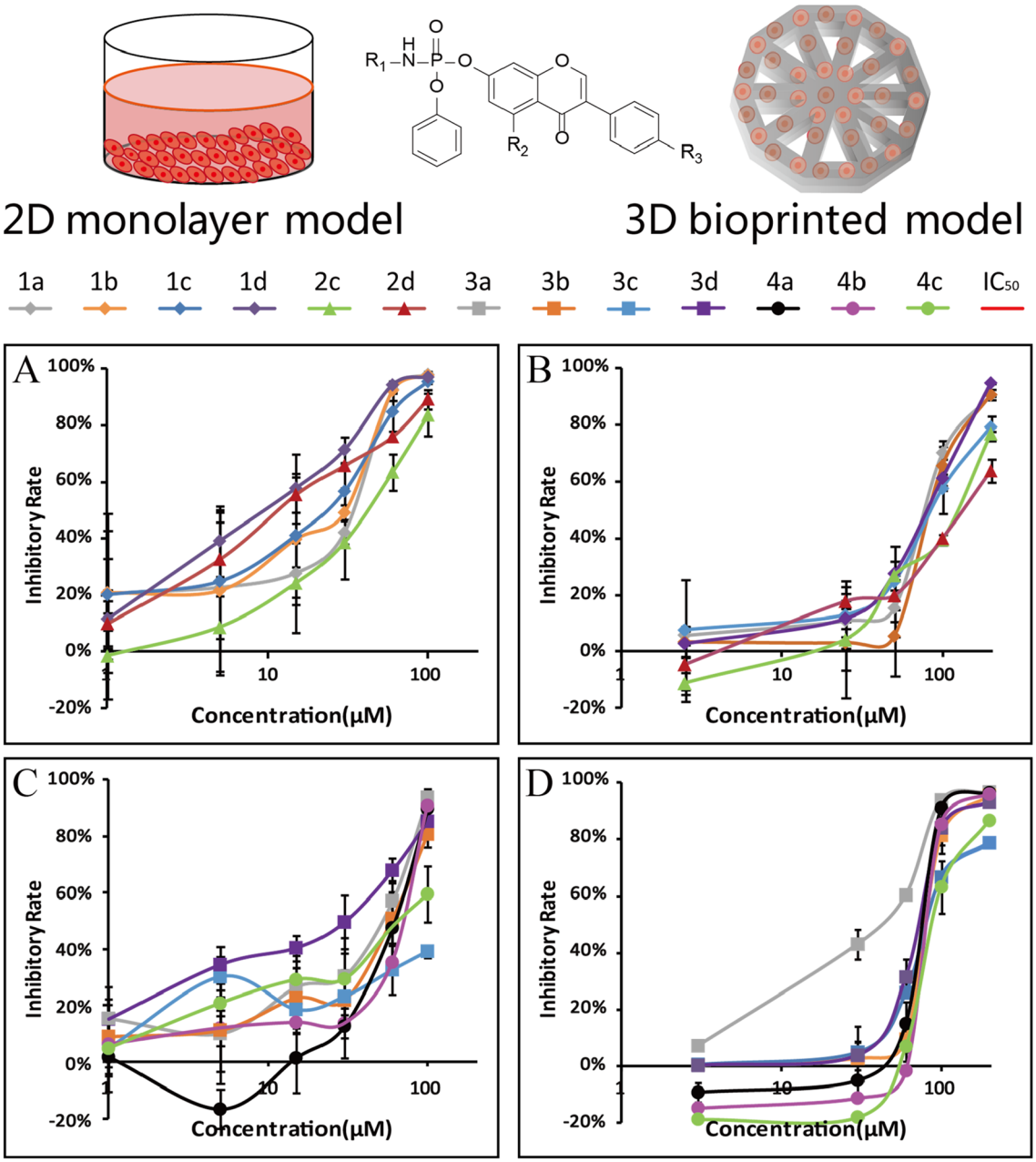

Fig. 5 Inhibition curves of 13 isoflavone derivatives against MCF-7 cells. **a** "Inhibition rate–concentration" curves of 1a, 1b, 1c, 1d, 2c, and 2d obtained with the 2D monolayer model; **b** "inhibition rate–concentration" curves of 1a, 1b, 1c, 1d, 2c and 2d obtained with the bioprinted 3D model; **c** "inhibition rate–concentration" curves of 3a, 3b, 3c, 3d, 4a, 4b, and 4c obtained with the 2D monolayer model; and **d** "inhibition rate–concentration" curves of 3a, 3b, 3c, 3d, 4a, 4b, and 4c obtained with the 3D bioprinted model. All data are presented as the mean ± standard deviation ($n = 4$)

simulates the microenvironment of a tumor as genuinely as possible; (2) it is stable when interacting with external drugs; and (3) it is easily standardized and manufactured for preclinical use.

Figure S1 in the supporting information shows the influence of microenvironments on the SAR study. We observed that, for the same drug candidates (1c, 1d, 2c), the SAR results varied between these three tumor spheroid models. The essential difference between these three spheroid models was the microenvironment, as listed in Table 2. We found that the HCSG-based bioprinted MCF-7 spheroid model was the most biomimetic model among these. We also tested the stability of the tumor spheroid models upon interacting with drugs. We observed that the matrixless spheroid model was not stable when interacting with drugs (Fig. S2 in the supporting information). However, we did not

Table 1 IC_{50}s of 13 isoflavone derivatives with the monolayer model and bioprinted model

No.	Substituents		Cell culture		
	Amino acid	Flavone	2D monolayer	3D bioprinted	3D/2D
IC_{50}(μM)					
1a	Phe	4′,5-diacetoxygenistein	34.6 ± 0.1	74.4 ± 0.9	2.15
3a	Phe	4′-acetoxydaidzein	52.3 ± 2.0	42.9 ± 1.5	0.82
4a	Phe	Daidzein	62.3 ± 0.6	77.0 ± 1.9	1.24
1b	Leu	4′,5-diacetoxygenistein	33.7 ± 1.1	93.3 ± 1.2	2.77
3b	Leu	4′-acetoxydaidzein	59.0 ± 1.6	78.9 ± 2.1	1.34
4b	Leu	Daidzein	71.6 ± 1.3	81.8 ± 1.4	1.14
1c	Gly	4′,5-diacetoxygenistein	30.1 ± 0.9	99.6 ± 2.6	3.31
2c	Gly	genistein	42.3 ± 1.9	109.2 ± 3.0	2.58
3c	Gly	4′-acetoxydaidzein	> 100	80.1 ± 0.8	< 0.8
4c	Gly	Daidzein	65.1 ± 0.4	87.5 ± 0.7	1.34
1d	Ala	4′,5-diacetoxygenistein	10.6 ± 0.7	78.5 ± 1.5	7.41
2d	Ala	Genistein	12.3 ± 1.3	166.6 ± 2.4	13.54
3d	Ala	4′-acetoxydaidzein	30.7 ± 0.8	72.9 ± 2.3	2.38
Erlotinib			7.8 ± 0.5	100.6 ± 1.6	12.90
5-FU			28.4 ± 1.1	287.7 ± 3.5	10.13
Doxorubicin			0.9 ± 0.1	2.6 ± 0.1	2.89

All data are presented as the mean ± standard deviation ($n = 4$)

observe disintegration of the tumor spheroids in the HCSG-based bioprinted MCF-7 spheroid models over the course of 15 days. Based on the results in Table 2 and Fig. S2, we found that the HCSG-based bioprinted spheroid model was not only highly biomimetic but also stable when interacting with drugs; thus, it is a suitable model for SAR study.

BME, for example, commercial Matrigel, has been considered as the standard biomaterial to mimic ECM around tumor cells in the body [23]. However, its printability is poor, and it is difficult to apply in 3D bioprinting. Sodium alginate/gelatin is one of the alternatives to BME in the field of 3D bioprinting because it is printable, biocompatible, cost-effective, and abundant in nature [24, 25]. However, SG is not perfect because its chemical components vary significantly with the extracellular matrix in vivo and because low printing temperatures result in many issues. The low temperature not only decreases the survival rate of cells but also increases the experimental difficulty of printing operations [26]. It can also change the mitochondria and rough endoplasmic reticulum morphology [27]. It can even affect cell mitochondrial activity, biogenesis and vascular endothelial growth factor expression in vitro [28, 29]. Wei Sun et al. partially alleviated the problem of SG by doping fibrinogen (8%) into the SG to enrich its chemical components [26], but the printing temperature remained a serious issue. In this study, we doped HEC into SG. HEC is a key component in HCSG. HEC is a nonionic hydrophilic polysaccharide biopolymer widely used in many medical applications due to its good biocompatibility and safety and its ability to stabilize and protect colloids [30–32]. HEC is very easy to disperse in cold or hot water, provided it a wide range of viscosity and non-thermal gel properties. Adding HEC to SG increased the viscosity of the low-concentration sodium alginate pregel solution and enhanced the gelation at 25 °C, resulting in an improved printability. We also found that when HEC was doped into SG, the key protein expressions of MCF-7 cells were similar to those in BME, validating the utilization of HCSG in an SAR study.

Table 2 Description of the microenvironments in three tumor spheroid models

Model	Microenvironment factors		
	Cell aggregation	Extracellular matrix	Vascularized tissue
Matrixless spheroid model	Yes	No	No
HCSG monolithic spheroid model	Yes	Yes	No
HCSG 3D bioprinted spheroid model	Yes	Yes	Yes

In fact, HCSG is different from the extracellular matrix in chemical components. It cannot perfectly simulate the intracellular matrix, as BME does. However, for the application of SAR studies, the key issue is the effect of the drug on the cell proliferation, vitality, etc. Thus, it is only necessary that the expression of proteins related to the proliferation, vitality, etc. in the HCSG be consistent with that in BME. As shown in Fig. 3, we observed this consistency; thus, HCSG

can be used to construct a biomimetic 3D spheroid model for SAR study.

Notably, the physiological behaviors of MCF-7 spheroids in the HCSG printed model were more active than in the monolithic model (Fig. 4). This is partially because the surface-area-to-volume ratio for the bioprinted model (Fig. S3 in supporting information) was much greater than that of the monolithic model (10 mm^{-1} vs. 2.05 mm^{-1}), resulting in a better mass transfer. The pores in the printed model were similar to the dense and rapidly growing vascular network in tumor tissues. The fast proliferation rate and the considerable mitochondrial metabolic activity in the bioprinted model fully conformed to the characteristics of rapid proliferation and high oxygen consumption of tumor tissues.

We analyzed and compared the SAR of isoflavone derivatives on a 2D monolayer culture and 3D spheroid model. As shown in Table 1, the SAR based on the matrixless spheroid model (1c > 2c > 1d) deviated from the SAR based on the HCSG spheroid models. This may be due to the instability of the spheroids, which fell apart after the drug acted.

The IC_{50}s of the isoflavone derivatives measured by the bioprinted model were relatively large because the tumor cells in the spheroid were not easily killed in the later stage, which was the same as for the tumor stem cells in vivo. The SAR of amino acid skeleton and isoflavone bone structure based on the 3D bioprinted MCF-7 spheroid model was different from that based on the 2D MCF-7 monolayer model. This suggests that drug molecules display different pharmacologies against 3D bioprinted models from that against a 2D monolayer culture. This phenomenon has also been reported elsewhere [11], possibly due to changes in cell phenotypes.

Conclusion

We developed a biomimetic 3D tumor spheroid model for the study of the structure–activity relationship in terms of phenotype. This spheroid model used a new biomaterial, hydroxyethyl cellulose/sodium alginate/gelatin (HCSG). The key protein expression of the MCF-7 cells in HCSG is similar to that of commercial BME. HCSG can also be printed at 25 °C to ensure a high cell viability. We studied the SAR of 13 isoflavone derivatives using the HCSG-based tumor model and identified the effects of acetylation and amino acid substituents on the activity and resistance of isoflavone derivatives. The alanine structure induced a stronger drug resistance, whereas phenylalanine barely caused drug resistance in the MCF-7 cells.

Acknowledgements This work was supported by the National Natural Science Foundation of China (No. 21675017), State Key Laboratory for Managing Biotic and Chemical Threats to the Quality and Safety of Agro-products (KF20190108), and the National Key Research and Development Program of China (No. 2017YFC1702001). And we thanked Prof. Yueqing Li for the synthesis of the isoflavone derivatives and useful discussions.

Author contributions Y. Luo and X.L. Zhang conceived this study. The manuscript was written through contributions of all authors. All authors have given approval to the final version of the manuscript. X.R. Li and Q.F. Deng contributed equally to this work.

Compliance with ethical standards

Conflict of interest The authors declare no conflict of interest.

Ethical Approval This study does not contain any studies with human or animal subjects performed by any of the authors.

References

1. Rohall SL, Auch L, Gable J, Gora J, Jansen J, Lu Y, Martin E, Pancost-Heidebrecht M, Shirley B, Stiefl N, Lindvall M (2020) An artificial intelligence approach to proactively inspire drug discovery with recommendations. J Med Chem. https://doi.org/10.1021/acs.jmedchem.9b02130
2. Li F, Cao L, Parikh S, Zuo R (2020) Three-dimensional spheroids with primary human liver cells and differential roles of kupffer cells in drug-induced liver injury. J Pharm Sci 109(6):1912–1923. https://doi.org/10.1016/j.xphs.2020.02.021
3. Beaurivage C, Naumovska E, Chang YX, Elstak ED, Nicolas A, Wouters H, van Moolenbroek G, Lanz HL, Trietsch SJ, Joore J, Vulto P, Janssen RAJ, Erdmann KS, Stallen J, Kurek D (2019) Development of a gut-on-a-chip model for high throughput disease modeling and drug discovery. Int J Mol Sci 20(22):5661. https://doi.org/10.3390/ijms20225661
4. Marotta N, Kim S, Krainc D (2020) Organoid and pluripotent stem cells in Parkinson's disease modeling: an expert view on their value to drug discovery. Expert Opin Drug Discov 15(4):427–441. https://doi.org/10.1080/17460441.2020.1703671
5. Gardin C, Ferroni L, Latremouille C, Chachques JC, Mitrecic D, Zavan B (2020) Recent applications of three dimensional printing in cardiovascular medicine. Cells. https://doi.org/10.3390/cells9030742
6. Zhao Y, Yao R, Ouyang L, Ding H, Zhang T, Zhang K, Cheng S, Sun W (2014) Three-dimensional printing of Hela cells for cervical tumor model in vitro. Biofabrication 6(3):035001. https://doi.org/10.1088/1758-5082/6/3/035001
7. King SM, Presnell SC, Nguyen DG (2014) Development of 3D bioprinted human breast cancer for in vitro drug screening. Cancer Res 74(19):5. https://doi.org/10.1158/1538-7445.am2014-2034
8. Brancato V, Oliveira JM, Correlo VM, Reis RL, Kundu SC (2020) Could 3D models of cancer enhance drug screening? Biomaterials 232:119744. https://doi.org/10.1016/j.biomaterials.2019.119744
9. Salib JY, El-Toumy SA, Hassan EM, Shafik NH, Abdel-Latif SM, Brouard I (2014) New quinoline alkaloid from Ruta graveolens aerial parts and evaluation of the antifertility activity. Nat Prod Res 28(17):1335–1342. https://doi.org/10.1080/14786419.2014.903395
10. Cos P, Ying L, Calomme M, Hu JP, Cimanga K, Van Poel B, Pieters L, Vlietinck AJ, Vanden Berghe D (1998) Structure–activity relationship and classification of flavonoids as inhibitors of xanthine oxidase and superoxide scavengers. J Nat Prod 61(1):71–76. https://doi.org/10.1021/np970237h

11. Wang J, Zhang X, Li X, Zhang Y, Hou T, Wei L, Qu L, Shi L, Liu Y, Zou L, Liang X (2016) Anti-gastric cancer activity in three-dimensional tumor spheroids of bufadienolides. Sci Rep 6:24772. https://doi.org/10.1038/srep24772
12. Albritton JL, Miller JS (2017) 3D bioprinting: improving in vitro models of metastasis with heterogeneous tumor microenvironments. Dis Model Mech 10(1):3–14. https://doi.org/10.1242/dmm.025049
13. Knowlton S, Onal S, Yu CH, Zhao JJ, Tasoglu S (2015) Bioprinting for cancer research. Trends Biotechnol 33(9):504–513. https://doi.org/10.1016/j.tibtech.2015.06.007
14. Meng F, Meyer CM, Joung D, Vallera DA, McAlpine MC, Panoskaltsis-Mortari A (2019) 3D bioprinted in vitro metastatic models via reconstruction of tumor microenvironments. Adv Mater 31:e1806899. https://doi.org/10.1002/adma.201806899
15. Zhang YS, Duchamp M, Oklu R, Ellisen LW, Langer R, Khademhosseini A (2016) Bioprinting the cancer microenvironment. ACS Biomater Sci Eng 2(10):1710–1721. https://doi.org/10.1021/acsbiomaterials.6b00246
16. Guestini F, Ono K, Miyashita M, Ishida T, Ohuchi N, Nakagawa S, Hirakawa H, Tamaki K, Ohi Y, Rai Y, Sagara Y, Sasano H, McNamara KM (2018) Impact of Topoisomerase IIalpha, PTEN, ABCC1/MRP1, and KI67 on triple-negative breast cancer patients treated with neoadjuvant chemotherapy. Breast Cancer Res Treat 173(2):275–288. https://doi.org/10.1007/s10549-018-4985-6
17. Zhang L, Wang L, Dong D, Wang Z, Ji W, Yu M, Zhang F, Niu R, Zhou Y (2018) MiR-34b/c-5p and the neurokinin-1 receptor regulate breast cancer cell proliferation and apoptosis. Cell Prolif 52(1):e12527. https://doi.org/10.1111/cpr.12527
18. Kaushal N, Tiruchinapally G, Durmaz YY, Bao L, Gilani R, Merajver SD, ElSayed MEH (2018) Synergistic inhibition of aggressive breast cancer cell migration and invasion by cytoplasmic delivery of anti-RhoC silencing RNA and presentation of EPPT1 peptide on "smart" particles. J Control Release 289:79–93. https://doi.org/10.1016/j.jconrel.2018.07.042
19. Islam F, Gopalan V, Lam AK, Kabir SR (2018) Pea lectin inhibits cell growth by inducing apoptosis in SW480 and SW48 cell lines. Int J Biol Macromol 117:1050–1057. https://doi.org/10.1016/j.ijbiomac.2018.06.021
20. Zhong C, Xie H-Y, Zhou L, Xu X, Zheng S-S (2016) Human hepatocytes loaded in 3D bioprinting generate mini-liver. Hepatobiliary Pancreat Dis Int 15(5):512–518. https://doi.org/10.1016/s1499-3872(16)60119-4
21. Pimentel CR, Ko SK, Caviglia C, Wolff A, Emneus J, Keller SS, Dufva M (2018) Three-dimensional fabrication of thick and densely populated soft constructs with complex and actively perfused channel network. Acta Biomater 65:174–184. https://doi.org/10.1016/j.actbio.2017.10.047
22. Li YQ, Yang F, Wang L, Cao Z, Han TJ, Duan ZA, Li Z, Zhao WJ (2016) Phosphoramidate protides of five flavones and their antiproliferative activity against HepG2 and L-O2 cell lines. Eur J Med Chem 112:196–208. https://doi.org/10.1016/j.ejmech.2016.02.012
23. Benton G, Kleinman HK, George J, Arnaoutova I (2011) Multiple uses of basement membrane-like matrix (BME/Matrigel) in vitro and in vivo with cancer cells. Int J Cancer 128(8):1751–1757. https://doi.org/10.1002/ijc.25781
24. Zehnder T, Sarker B, Boccaccini AR, Detsch R (2015) Evaluation of an alginate-gelatine crosslinked hydrogel for bioplotting. Biofabrication 7(2):025001. https://doi.org/10.1016/j.biomaterials.2015.05.031
25. Neufurth M, Wang X, Schroder HC, Feng Q, Diehl-Seifert B, Ziebart T, Steffen R, Wang S, Muller WEG (2014) Engineering a morphogenetically active hydrogel for bioprinting of bioartificial tissue derived from human osteoblast-like SaOS-2 cells. Biomaterials 35(31):8810–8819. https://doi.org/10.1016/j.biomaterials.2014.07.002
26. Ouyang L, Yao R, Chen X, Na J, Sun W (2015) 3D printing of HEK 293FT cell-laden hydrogel into macroporous constructs with high cell viability and normal biological functions. Biofabrication 7(1):015010. https://doi.org/10.1088/1758-5090/7/1/015010
27. Saito M, Shinbo T, Saito T, Kato H, Otagiri H, Karaki Y, Tazawa K, Fujimaki M (1990) Temperature sensitivity on proliferation and morphologic alteration of human esophageal carcinoma cells in culture. Vitro Cell Dev Biol 26(2):181–186. https://doi.org/10.1007/BF02624110
28. Sugasawa T, Mukai N, Tamura K, Tamba T, Mori S, Miyashiro Y, Yamaguchi M, Nissato S, Ra S, Yoshida Y, Hoshino M, Ohmori H, Kawakami Y, Takekoshi K (2016) Effects of cold stimulation on mitochondrial activity and VEGF expression in vitro. Int J Sports Med 37(10):766–778. https://doi.org/10.1055/s-0042-102659
29. Yasuhara R, Kushida R, Ishii S, Yamanoha B, Shimizu A (2013) Effects of pressure and temperature on the survival rate of adherent A-172 cells. High Press Res 33(2):322–327. https://doi.org/10.1080/08957959.2013.780054
30. Kamel S, Ali N, Jahangir K, Shah SM, El-Gendy AA (2008) Pharmaceutical significance of cellulose: a review. Express Polym Lett 2(11):758–778. https://doi.org/10.3144/expresspolymlett.2008.90
31. Zulkifli FH, Hussain FS, Rasad MS, Mohd Yusoff M (2014) Nanostructured materials from hydroxyethyl cellulose for skin tissue engineering. Carbohydr Polym 114:238–245. https://doi.org/10.1016/j.carbpol.2014.08.019
32. Chahal S, Hussain FSJ, Yusoff MM, Abdull Rasad MSB, Kumar A (2016) Nanohydroxyapatite-coated hydroxyethyl cellulose/poly (vinyl) alcohol electrospun scaffolds and their cellular response. Int J Polym Mater Polym Biomater 66(3):115–122. https://doi.org/10.1080/00914037.2016.1190926